



**HAL**  
open science

# The transient electromagnetic (TEM) method reveals the role of tectonic faults in seawater intrusion at Zhoushan islands (Hangzhou Bay, China)

Zhongmin Zhu, Zhigang Shan, Yonghao Pang, Wei Wang, Mei Chen,  
Guangchang Li, Huaifeng Sun, André Revil

## ► To cite this version:

Zhongmin Zhu, Zhigang Shan, Yonghao Pang, Wei Wang, Mei Chen, et al.. The transient electromagnetic (TEM) method reveals the role of tectonic faults in seawater intrusion at Zhoushan islands (Hangzhou Bay, China). *Engineering Geology*, 2024, 330, 10.1016/j.enggeo.2024.107425 . hal-04540593

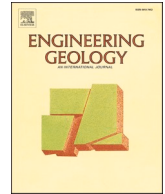
**HAL Id: hal-04540593**

**<https://hal.science/hal-04540593>**

Submitted on 10 Apr 2024

**HAL** is a multi-disciplinary open access archive for the deposit and dissemination of scientific research documents, whether they are published or not. The documents may come from teaching and research institutions in France or abroad, or from public or private research centers.

L'archive ouverte pluridisciplinaire **HAL**, est destinée au dépôt et à la diffusion de documents scientifiques de niveau recherche, publiés ou non, émanant des établissements d'enseignement et de recherche français ou étrangers, des laboratoires publics ou privés.



# The transient electromagnetic (TEM) method reveals the role of tectonic faults in seawater intrusion at Zhoushan islands (Hangzhou Bay, China)

Zhongmin Zhu<sup>a,b</sup>, Zhigang Shan<sup>b</sup>, Yonghao Pang<sup>b,c</sup>, Wei Wang<sup>b</sup>, Mei Chen<sup>b</sup>, Guangchang Li<sup>b</sup>, Huaifeng Sun<sup>c</sup>, André Revil<sup>d,\*</sup>

<sup>a</sup> Institute of Polar and Ocean Technology, Second Institute of Oceanography, MNR, Hangzhou 310012, China

<sup>b</sup> Zhejiang Huadong Geotechnical Investigation & Design Institute CO., LTD, Hangzhou 310023, China

<sup>c</sup> Geotechnical and Structural Engineering Research Center, Shandong University, Jinan 250100, China

<sup>d</sup> Université Grenoble Alpes, Université Savoie Mont-Blanc, CNRS, UMR CNRS 5204, EDYTEM, 73370 Le Bourget du Lac, France

## ARTICLE INFO

### Keywords:

Seawater intrusion  
Small loop time domain electromagnetic  
Quasi-3D mapping

## ABSTRACT

Seawater intrusion into onshore aquifers represents a significant environmental threat worldwide especially in this new era of climate change and sea water rise. This is the case at the Zhoushan Islands located in Hangzhou Bay (China). Precise monitoring of the position of the boundary between freshwater and saltwater is of utmost importance for water resource management especially in fractured bedrock. We use the Transient ElectroMagnetic (TEM) method to locate a salt plume in an area where two sets of faults-oriented NW-SE and NE-SW are connected to the sea in a rhyolitic substratum. The survey comprises 558 Transient ElectroMagnetic (TEM) soundings. The inverted resistivity data are combined with borehole logging data to underline the areas of groundwater salt concentration in the aquifer. This salinization is taking place along the pervasive fault zones indicating the role of these faults in channeling the salty water through the rhyolitic bedrock. This study underlines the critical role of faults pathways in the groundwater mineralization issues faced by coastal aquifers in fractured crystalline substratum.

## 1. Introduction

Ground water quality in coastal areas is endangered by salt water intrusion especially in the face of climate change and sea-level rise (e.g., Qasim et al., 2022; Panthi et al., 2022; Wang et al., 2022). Adequate resource managements imply the monitoring of the position of the saltwater front (Barlow, 2003; Seibert et al., 2023). Indeed, gaining insights into the position and dynamics of the salt water front enables managers to make informed decisions aimed at safeguarding water-supply wells and mitigating additional intrusion (Amer et al., 2023). The dynamics of sea water intrusion is however complex with a lot parameters being able to influence its position over time (e.g., Dhal and Swain, 2022; Lo and Sangare, 2023; Luo et al., 2023). The problem is especially important in small islands regarding drinking water management (Kura et al., 2014; Kumar and Mukherjee, 2023; Sharan et al., 2023). Ground water flow in fractured aquifers is somehow tricky to observe because of the high degree of heterogeneity of such systems (Bense and Person, 2006). However, to our knowledge, the role of

tectonic faults in channeling salty water in the substratum of coastal areas has not been addressed so far.

Geophysical methods can play a critical role in delineating the position of sea water intrusions (e.g., Adeyemo et al., 2022). In recent years, the Transient ElectroMagnetic (TEM) method has gained popularity as a non-invasive and efficient technique in hydrogeophysics (e.g., Knight et al., 2022). The TEM method has been employed in diverse applications, encompassing the identification of potential sites for groundwater recharge and the investigation of seawater intrusion issues (Goebel et al., 2019). The airborne electromagnetic method has been utilized to locate and map deposits along the eastern edge of the Central Valley, with the objective of identifying favorable areas for groundwater recharge (Knight et al., 2022). This technique enables potential locations conducive to recharge, thereby supporting the sustainable management of groundwater resources (Kang et al., 2022; Knight et al., 2022; Gottschalk et al., 2020). In coastal regions, the ground-based TEM-technique with large loops (typically 50 × 50 m) has been employed to investigate issues related to seawater intrusion (Kalisperi

\* Corresponding author.

E-mail addresses: [zhuzm@sio.org.cn](mailto:zhuzm@sio.org.cn) (Z. Zhu), [shan\\_zg@hdec.com](mailto:shan_zg@hdec.com) (Z. Shan), [pang\\_yh1@hdec.com](mailto:pang_yh1@hdec.com) (Y. Pang), [wang\\_w20@hdec.com](mailto:wang_w20@hdec.com) (W. Wang), [chen\\_m3@hdec.com](mailto:chen_m3@hdec.com) (M. Chen), [li\\_gc@hdec.com](mailto:li_gc@hdec.com) (G. Li), [sunhuaifeng@email.sdu.edu.cn](mailto:sunhuaifeng@email.sdu.edu.cn) (H. Sun), [andre.revil@univ-smb.fr](mailto:andre.revil@univ-smb.fr) (A. Revil).

<https://doi.org/10.1016/j.enggeo.2024.107425>

Received 30 November 2023; Received in revised form 22 January 2024; Accepted 24 January 2024

Available online 1 February 2024

0013-7952/© 2024 Published by Elsevier B.V.

et al., 2018). By analyzing the subsurface conductive characteristics, this method helps in identifying areas influenced by the dynamics of seawater intrusion.

For near-surface applications (depths less than 70 m), we need dense surveys that can be performed in a short period of time in order to get highly detailed interpretations for surface recharge. A towed Transient ElectroMagnetic (tTEM) system has been specifically designed for such problem and used here for the first time. The tTEM system has a shallower focus depth compared to traditional TEM systems due to its smaller size (Auken et al., 2019; Christensen, 2014). It is capable of imaging the uppermost 70 m of the subsurface with high resolution, facilitated by the small footprint of the system with respect to galvanometric methods and dense data collection patterns. It complements galvanometric method such as DC (Direct Current) resistivity and induced polarization techniques (e.g., Binley et al., 2015) and the self-potential (passive) technique (e.g., Revil et al., 2005).

The TEM technique is efficient, providing rapid and detailed subsurface imaging over large areas (Maurya et al., 2020; Lane et al., 2020; Kang et al., 2022). It also allows for the collection of data at various depths, providing valuable insights into the distribution and movement of groundwater. The detailed 3D geological models provide a comprehensive understanding of the subsurface hydrogeological system. They capture the complex geological structures including aquifers (Knight et al., 2022), aquitards, faults, and fractures (Auken et al., 2019), which influence the movement and distribution of groundwater. By incorporating geological data at different scales, including lithology, stratigraphy, and structural information, these models enable a more realistic representation of the subsurface. To enhance the imaging of hydrogeological structures, various constrained approaches have been employed in TEM inversion. The Spatially Constrained Inversion (SCI) technique incorporates smooth assumptions regarding the spatial variability of the subsurface properties into the inversion process (Viezzoli et al., 2009). It utilizes regularization techniques to enforce smoothness or continuity in the estimated 2D/3D model while honoring the recorded data. In some cases, when additional prior information or knowledge about the subsurface is available, it could be incorporated into the inversion by using a multi-step inversion process that incorporates both the standard  $l_2$ -norm inversion and the  $l_p$ -norm inversion to obtain more accurate and realistic models (Kang et al., 2022). The high data coverage system and the improved imaging approach makes the TEM method highly suitable for mapping details to be used in 3D geological models aimed at aquifer mapping and seawater intrusion assessments (Delsman et al., 2018).

While extensive research has been dedicated to understanding seawater intrusion in coastal aquifers, particularly in sedimentary formations, a glaring gap persists in the imaging of saltwater flow pathways within fractured aquifers. Despite the advancements in geophysical methods, such as electrical resistivity tomography and airborne electromagnetic techniques, their application to accurately visualize and map the intricate flow pathways in fractured aquifers remains largely uncharted. Our goal is to show that the TEM method is adequate in providing the necessary information to reveal the role of faults in channeling sea water inland.

## 2. Method

### 2.1. Small loop TEM system—FCTEM

The TEM method employs a primary current waveform transmitted into the subsurface through a loop (Auken et al., 2009), this process induces eddy currents and a temporary magnetic field. By measuring the decay of the magnetic field over time, TEM can provide valuable insights into the subsurface electrical conductivity distribution, which is sensitive to salinity, water and clay contents.

An ideal TEM system should be compact, lightweight, and possess a small footprint while delivering ample transmitter power to investigate

the subsurface electrical properties (Sandersen et al., 2021). FCTEM is a newly designed small loop (with diameter about 1.1 m) TEM system, shown in Fig. 1. To enhance the Depth Of Investigation (DOI), the peak transient current is raised to 60 A, and the number of loops in the Tx coil is increased to 33. The receiver coil features an effective area of 4 m<sup>2</sup> with a bandwidth of 100 kHz. Due to the system's small transmitter loop (with a diameter of 1.1 m), it offers a compact footprint and enables dense data collection, distinguishing it from traditional ground-based TDEM methods. Modelling in Fig. 2 demonstrates that the use of a small Tx loop enhances vertical resolution.

When the primary current is turned off, eddy currents are induced in the conductive block, leading to an increase in the observed decay (Fig. 2a). When the Tx loop is comparable or smaller than the lateral geometry of the conductive block, the normalized detection capacity can increase by a factor of ten compared to using a large loop.

### 2.2. Spatially constrained inversion for TEM data

To take full advantage of the spatial coherency in the TEM data, Spatially Constrained Inversion (SCI) is utilized to recover quasi-3D geoelectrical model. The crucial aspect of utilizing the SCI is the construction of a regular matrix that incorporates the spatial relationship between neighboring soundings. For the inversions of all TME soundings, we use the following objective function

$$\begin{aligned} \phi(\mathbf{m}) &= \phi_d(\mathbf{m}) + \beta \phi_m(\mathbf{m}) \\ &= \|w_d(\mathbf{d}_{pre} - \mathbf{d}_{obs})\| + \beta \left( \alpha_s \|w_s^{cell}(\mathbf{m} - \mathbf{m}_{ref})\| + \alpha_r \left\| w_r^{cell} \frac{d\mathbf{m}}{dr} \right\| + \alpha_z \left\| w_z^{cell} \frac{d\mathbf{m}}{dz} \right\| \right) \end{aligned} \quad (1)$$

where  $\phi_d(\mathbf{m})$  is the data misfit term,  $\phi_m(\mathbf{m})$  denotes the regularization term of the cost function and  $\mathbf{m}$  denotes the model vector. The first term of the regularization function  $\phi_m(\mathbf{m})$  corresponds to a minimum norm constraint. The two other terms of  $\phi_m(\mathbf{m})$  denote spatial constraints, one acting in the vertical ( $z$ -)direction, and the other in the lateral direction (denoted by  $r$ ). In Eq. (1),  $\mathbf{m}$  and  $\mathbf{m}_{ref}$  represent the resistivity model we try to recover and a reference model at each sounding position, respectively. The three parameters  $\alpha_s$ ,  $\alpha_z$ ,  $\alpha_r$ , determine the relative importance of each constrain in the regularization term. We use the open source SimpegEM1D to achieve constrained inversion (see details in Cockett et al., 2015). In consideration of the layered materials present in the study area,  $\alpha_z$  was set to ten times smaller than  $\alpha_r$  to emphasize our preference for laterally continuous rather than vertically continuous structure and  $\alpha_r$  was fixed to 1 by default.

Cell-based weightings for the two spatial constraints  $w_z^{cell}$  and  $w_r^{cell}$  were used to minimize the model variations in the vertical and lateral directions for cells. Since the layer thickness of all soundings are fixed, the vertical spatial constraints  $w_r^{cell}$  remain fixed. While the lateral weightings constraints can be set between any cells. The values of these weightings depend on the distribution of all sounding points. Adjoint soundings prefer larger weightings to selected neighboring cells than to other cells resulting in smaller resistivity variations. The nearest neighbor of each cell could be determined using Delaunay triangulation. This process generates the weightings for each central cell until all soundings are included in the matrix  $w_r^{cell}$ . The resulting regular matrix allows for the minimization of resistivity variations along and across profiles.

### 2.3. Layered inversion involved waveforms

In actually implement scenario, transmitter current produced in the Tx loop is critical ingredients of measured electromagnetic response. The shape of current waveform depends highly on the specific TEM system. The induced current diffusion fast into subsurface, and the key parameter dominate resolution is turn off time and delay time (the first time gate to recording unbiased signal) (Auken et al., 2019). Observed



**Fig. 1.** The small loop TEM system FCTEM used in this study. Inside the white plastic package are the transmitting and receiving coils, and the diameter of the transmitting coil is 1.1 m.

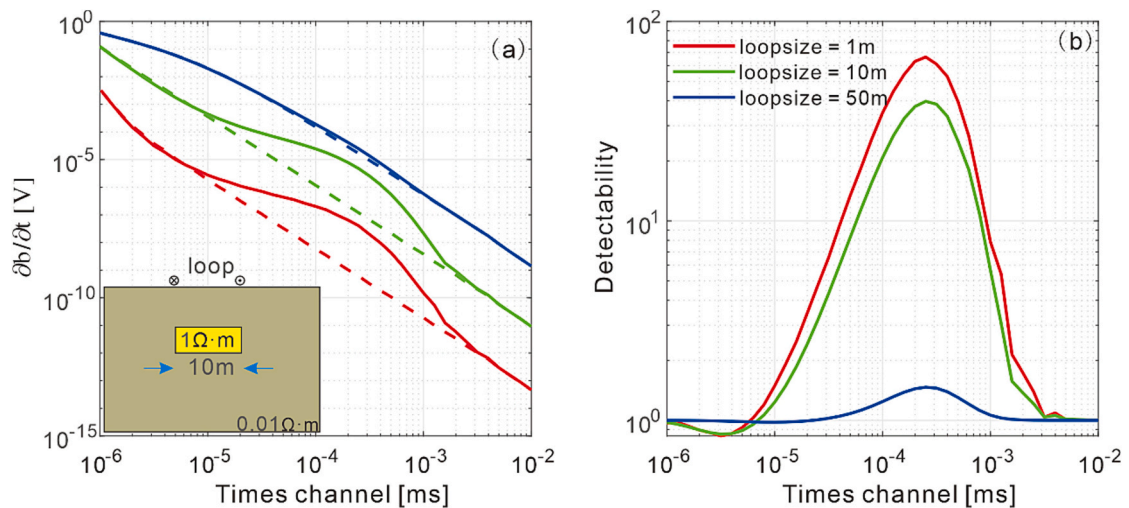


**Fig. 2.** Central loop response of different transmit loop size. (a) Time decay of voltage in the central coil with varies loop radius. (b) Normalized detective capability for different loop size. Solid line shows in-loop response with block anomaly. Finally, the dashed line denotes the background response without the conductive block.

signal involved arbitrary current waveform could be defined as the convolution of the impulse responses for layered model and the time derivative of transmitter current (Auken et al., 2020). This convolution could be evaluated by the Gaussian quadrature. The detail of

computation strategy could be found in various papers such as Yin et al. (2008) and Auken et al. (2020). Here we implement the convolution to the actual source current to validate the resolve capacity of small loop TEM.

Measured actual current waveform of FCTEM is shown in Fig. 3a. The presence of the 33 loop turns results in a turn off time at  $\sim 120 \mu\text{s}$ , and there is a significant current oscillation during the early shutdown due to the high-speed switching. Using the full wave modelling scheme allow us to calculate the data response after the Tx turned off and evaluate the effect of practical waveforms. The longer turn off time effect the decay rate of magnetic diffusion into earth, leading to a decrease in induced voltage in the central coil during the early time gates (blue lines in Fig. 3 b). These decay rates reflect the change of turn off, as expected. Furthermore, the current oscillations at  $\sim 115 \mu\text{s}$  results in a sign reversal of observed transients in the time gate range 4–30  $\mu\text{s}$ , exhibiting a positive-negative-positive decay pattern, and in practice, the data recording typically begins at around 32  $\mu\text{s}$ .

To demonstrate model resolution of different waveforms, a synthetic resistivity model with thin layer and stair conductive anomaly was built. A 20  $\Omega\text{-m}$  thin layer above 10  $\Omega\text{-m}$  stair blocks in a 100  $\Omega\text{-m}$  background. The thickness of layers varying from 10 to 40 m over a distance of 50 m. We calculate the synthetic data for every 5 m and apply 3% uncertainties to the observed (numerically computed) data. Two typical synthetic datasets are calculated using step off waveform and actual waveform measured form the TEM systems. Then; the datasets are inverted using the SCI technique as described above, with their respective waveforms. Layered model to be inverted is log resistivity values defined in 30 vertical layers, with a thickness of 2 m for the first layer of the surface, increasing by a constant factor, leading to a total depth of 176 m. The inversion is carried out using the Simpeg-EM1D algorithm (Heagy et al., 2017), with vertical constraint  $\alpha_z$  by 1 and lateral constraint  $\alpha_r$  by 10. Inversion parameter and the source current used in synthetic modelling is the same as in the field work described below.

The inverted results, which account for different waveforms, are shown in Fig. 4. For each case, single sounding curves demonstrate a good fit between all predicted data and the synthetic observed data. In an ideal scenario where a step-off waveform exists and data can be recorded immediately after the current ramp down, both the turn-off time and delay time are assumed to be zero. The estimated model closely resembles the true model as shown in Fig. 4c. The top shallow conductive layer can be clearly resolved. However, in practical cases, the current waveform has a turn-off time of approximately 120  $\mu\text{s}$ , and the observed data within the time gates range of 1–30  $\mu\text{s}$  are distorted by the primary current. To evaluate the effect of the early time gates, the

inversion scheme is performed with and without the distorted data. The inversion includes the time gates below 30  $\mu\text{s}$ , as presented in Fig. 4f, while the first gate time for the inversion results without the distorted data is approximately 32  $\mu\text{s}$ , as shown in Fig. 4i.

The two estimated models exhibit similar resistivity structures in the deeper part, with a focus on the top thin layer. The estimated model with early gates can identify the presence of the conductive layer, although the transition region between the thin layer and the underlying conductor is not clearly defined. In contrast, the inversion results obtained only with unbiased data struggle to distinguish the shallow conductive structures. The absence of these early gates weakens the resolution of the shallow layers, resulting in the transient system resolving only the average resistivity instead of individual layers.

Layered inversion involving waveforms, enables the utilization of early distorted data to enhance the resolution of the very shallow part of the geological structure. During the field data acquisition at this stage, distorted data before 32  $\mu\text{s}$  are disregarded, and only unbiased data are collected and used in the inversion procedure. In this context, the inversion takes into account waveforms as a means of calibrating the system response. Although this sacrifices shallow resolution, it accurately reconstructs deep conductive structures comparable to the expected depth of seawater intrusion.

### 3. Field application

#### 3.1. Geological setting

The study area for our field test is located in the northwestern region of Zhoushan Archipelago, characterized by a low mountain and hills terrain Zhejiang Province. The field exhibits significant undulations with an elevation range between sea surface to 120 m a.s.l. The geology of Cezi primarily consists of spotted rhyolites formed in lower Jurassic Period. The rhyolites are covered by Quaternary sediments. The local tectonic regime of this region is mainly characterized by two normal faults in NW-SE and NE-SW directions (labeled Fault1 and Fault2 in Fig. 5.). According to regional tectonic analysis, no active faults remain since the Late Pleistocene in the study area. Outcrop fracture zone is strongly-weathered, mainly composed of rock fragments and fault gouges, and the part of Fault1 near the sea has collapsed.

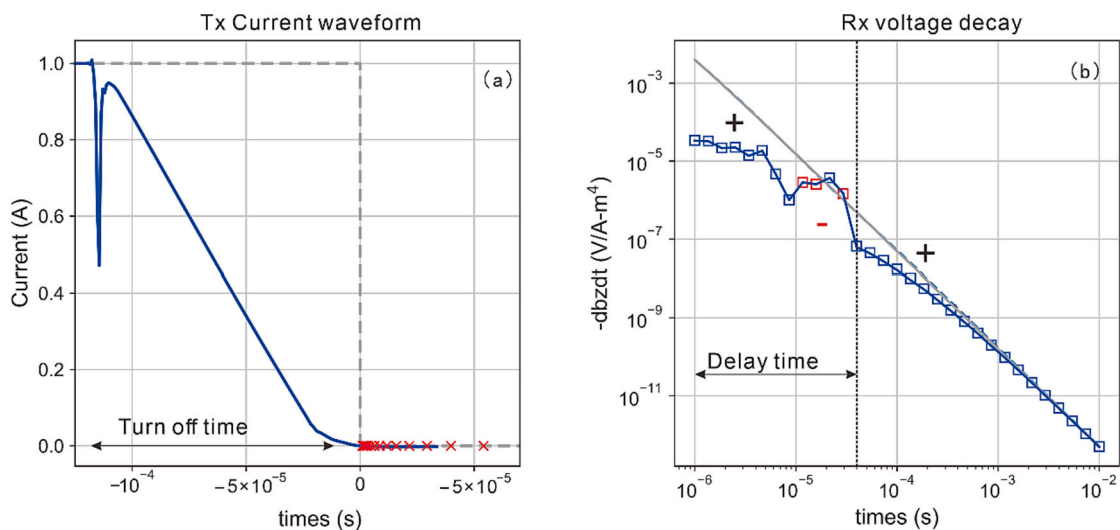


**Fig. 3.** Two current waveforms and synthetic convolution response. (a) Measured turn off waveform of the FCTEM system normalized by the peak current is shown in blue and the ideal step off current shown in grey, red cross denote the record time gates. (b) The blue line is the resulting calculated of receiver coil system response just after the current ramp-down. Red dots are negative. (For interpretation of the references to colour in this figure legend, the reader is referred to the web version of this article.)

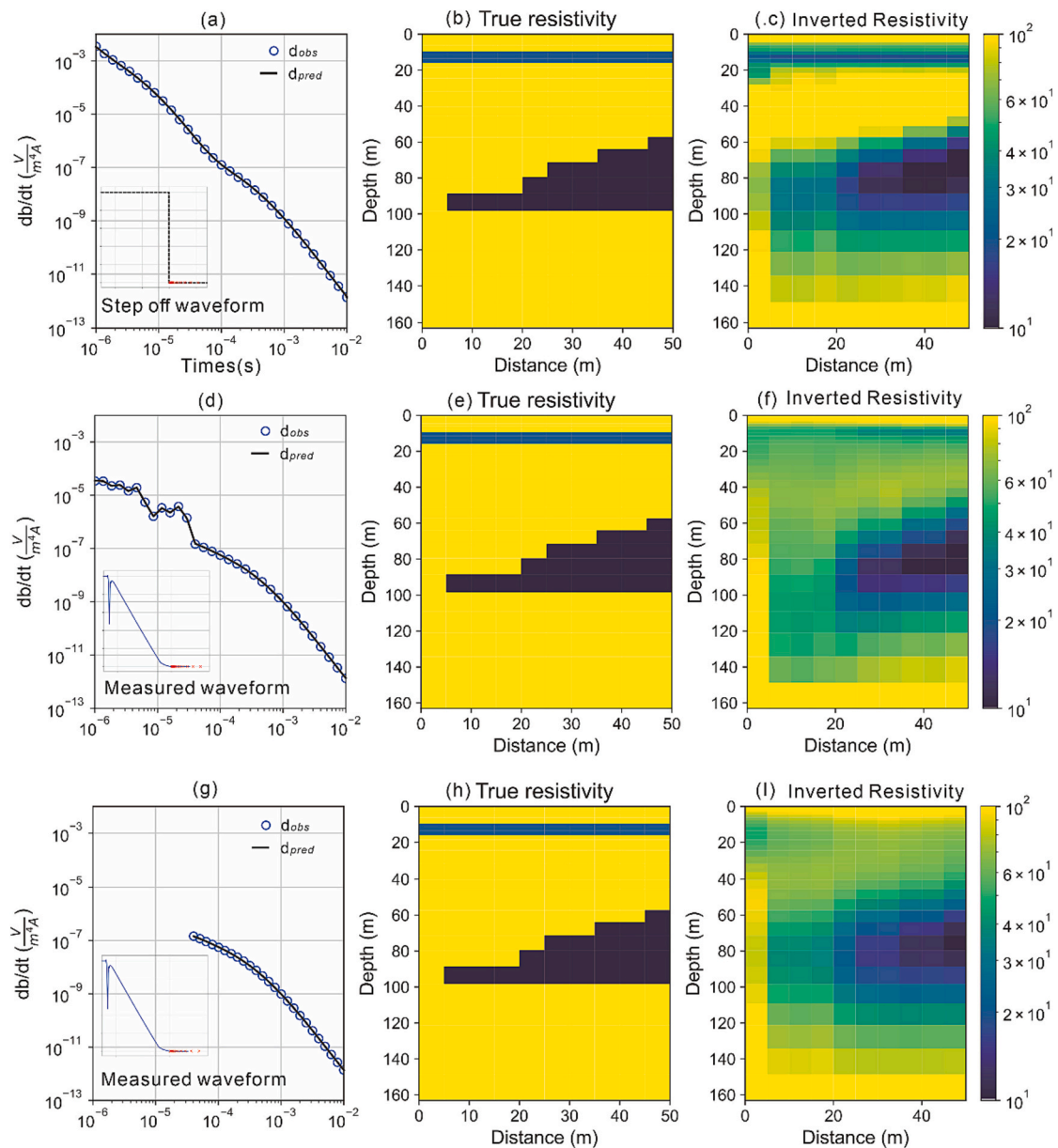


**Fig. 4.** Inversion results of synthetic model. (a) Sounding curves with an ideal step off waveform, black line is prediction response using estimated model in c; (b) True model; (c) Estimated model using step off waveform, including all time gates data; (d) Sounding curves corresponding to actual wave, black line is prediction response using estimated model in f; (e) True model; (f) Estimated model using actual waveform, inversion including early time distorted data (data from 1  $\mu$ s to 10 ms); (g) Sounding curves corresponding to actual waveform without early time distorted data, black line is prediction response using estimated model in f; (h) True model; (i) Estimated model using actual waveform involved inversion, with data from 32  $\mu$ s to 10 ms, excluding early time distorted data.

### 3.2. Hydrogeological setting

The hydrogeological setting of Cezi Island remains poorly investigated. The outcrops in the study area mainly consist of rhyolites, characterized by a dense compressive structure and weak permeability. However, geological mapping and drilling core analysis indicate a higher development of vertical joint fractures within the bedrock increasing locally the transmissivity of the material. These bedrocks contain water primarily in the fractures and cracks other than rock matrix. Consequently, the fluctuation of the aquifer and aquitard in this layer lacks a regular pattern due to significant water level fluctuations. The water table in the surveyed area varies greatly with the topography. Borehole statistics reveal that the water level elevation in the mountain area ranges mainly from 4 m to 57 m, while in the foothills, it is primarily between  $-0.6$  m and 4.4 m. The water level of the river on the

west side of the survey area is approximately 1 m. The study area is a humid region with a mean annual precipitation of 1410.8 mm. Small springs emerge in the western portion of the study area, with spring water originating from the accumulation of pore water from bedrock fractures and overburden sediments. This indicates that the surface sediments in the mountains serve as important shallow aquifers in this area, while the development of faults and fractures dominates the deep aquifers.

The groundwater in the field is typically tasteless, transparent, and of good quality. However, groundwater extracted near the coastline has shown to be slightly salty and astringent in recent years, likely due to the proximity of the wells to seawater. The direct pumping by villagers may have caused inland migration of the salty and freshwater transition zone, leading to the deterioration of water quality. We conducted a water quality analysis on various water samples from the research area

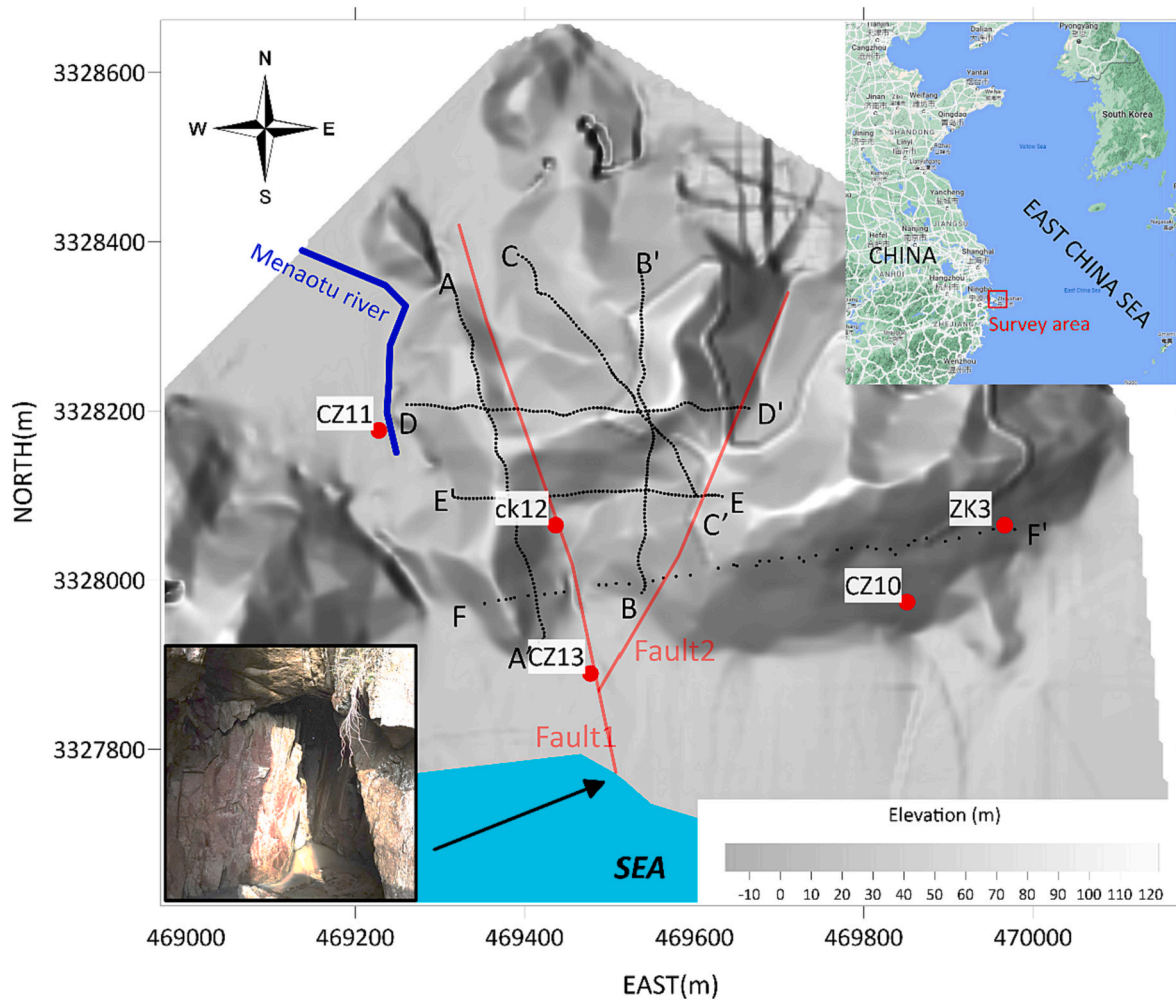


Fig. 5. Topography and geological map of study area, located northwestern of Zhoushan group islands. Red solid lines indicate certain faults, controlled by region geology (the photo shows the exposed Fault 1 near the coast), black dots are TEM soundings, ck denotes the location of the six boreholes. A-A' to F-F' indicates the position of the geophysical profiles. (For interpretation of the references to colour in this figure legend, the reader is referred to the web version of this article.)

(See Table 1).

The Menaotu River, situated on the northwest side of the study zone, connects directly to the sea through a sluice gate. Due to seawater influence, its chloride ion concentration is markedly higher than typical surface freshwater, the river's total dissolved solids (TDS) reached 5400 mg/L, while standard surface freshwater usually has a TDS less than 300 mg/L. The water samples from boreholes CZ11 and CZ13 exhibited a TDS value of 2400 mg/L. Given these data, it is likely that the groundwater in the region has been affected by seawater intrusion. Furthermore, we point out that CZ13 is located directly on a fault zone.

### 3.3. Transients data collection

The TEM data were acquired in November 2022 using small loop TEM system. Six TEM survey lines are show in Fig. 5. The southern boundary of the survey is located about 100 m of coast line of Hangzhou Bay and extends about 600 m to the north of residential area of the town. Sampling interval of TEM soundings is ~5 m. The decay of the magnetic field over a time gates range of 32 μs to 2 ms at logarithmic intervals was recorded for a total of 100 observed data points, and the raw data were stacked 200 times, with the estimated error are used as the uncertainties to invert 1D vertical resistivity profile at every sounding location.

Table 1

TDS of water samples from surface water and boreholes.

Item	Boreholes				Menaotu river	Surface groundwater	Seawater
	CZ13	CZ10	CZ11	Zk3			
CL <sup>-</sup>	1222.88	43.67	1153.9	57.4	3088.4	19.65–129.15	14,740–15,302
SO <sub>4</sub> <sup>2-</sup>	186.28	100.13	170.76	105.56	273.17	23.69–63.38	1453–1322
Ca <sup>2+</sup>	85.82	30.77	68.01	36.27	133.13	5.54–22.54	607–729
Mg <sup>2+</sup>	21.6	10.6	22.58	10.8	160.3	6.72–24.11	731–878
pH	7.95	7.17	7.61	7.27	8	7.2	8.63
TDS (mg/L)	2396	284	2248	324	5432	152.8–339.3	25,788–26,687
EC (μS/cm)	3422.14	406.29	3210.7	463.42	/	/	/

Note: The electrical conductivity (EC) of the pore water is calculated according to  $EC(\mu S/cm) = TDS(mg/L)/0.7$ .

4. Results and discussion

For Quasi-2D imaging of 1D geoelectric models, six sections were constructed using SCI form observed transient response. Driller's logs within 70 m are also displayed. The E-E' section (Fig. 6a) spans approximately 360 m long in W-E direction and it comprise the two major units covered by Quaternary sediments. Two faults with two distinct resistivity transition zone were recognized at the distance of 60 m and 220 m along geoelectrical model. The central part of the profile is defined well with the resistivity less than 60 Ω·m. Sediments which are

composed by gravel-bearing clay have resistivity ranging from 30 to 60 Ω·m. In general, sufficiently thick sediments could be identified from bed-rock because of the rich clay and porous water, although the TEM method has poor resolution for shallow surfaces. The fault observed in the profile are verified by surface geological investigation. And resistivity transition zone at the eastern part of profile is in good correlation with the core sample from borehole CK12. The core fracture zone in the bore shows steeply dipping fractures with chlorite and white calcareous films visible on the fracture surface and quartz fillings at individual fractures. In addition, the lower resistivity zone at depth

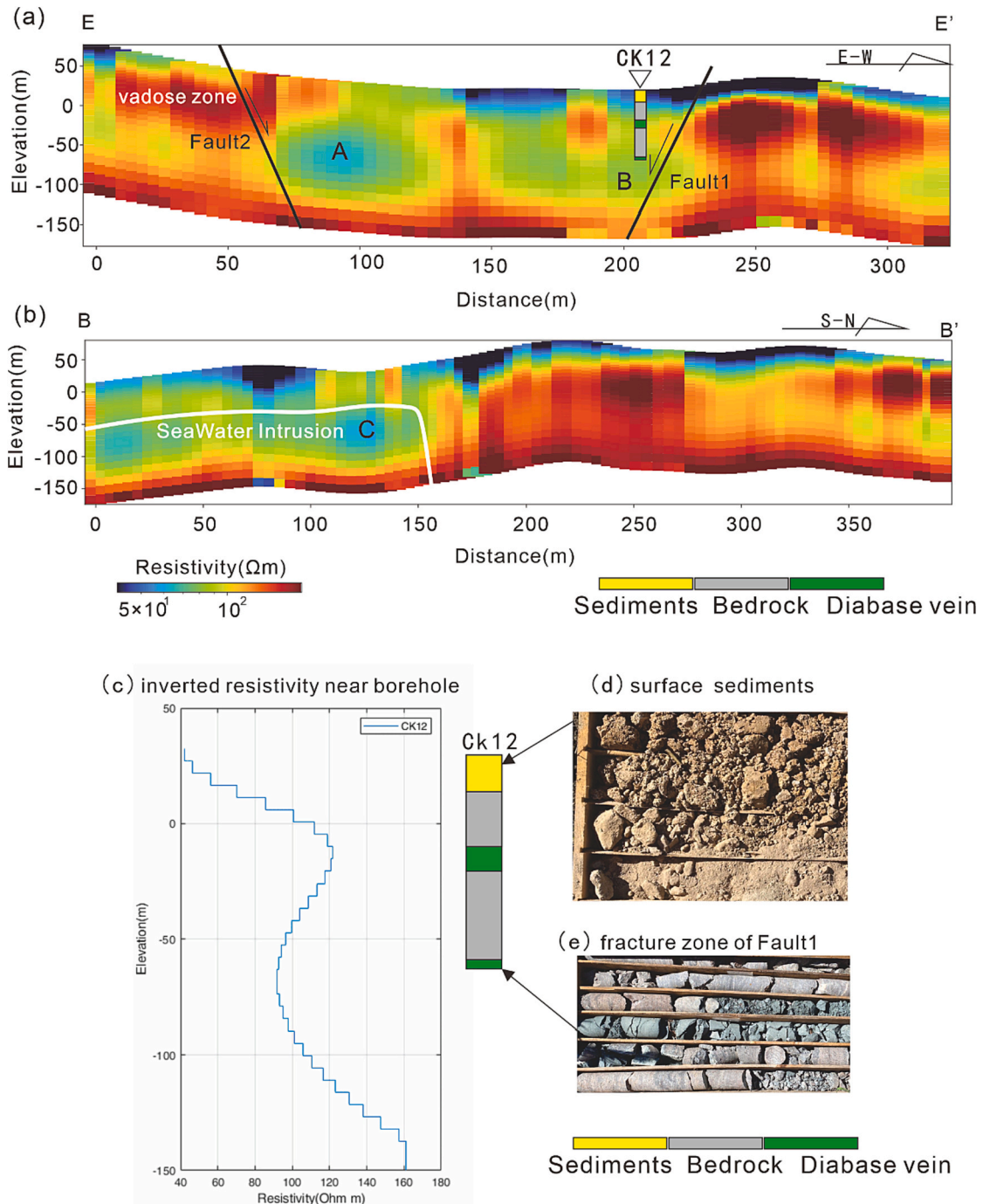


Fig. 6. Inversion profile of B-B' and E-E'. (a) resistivity distribution of E-E'; Black lines denotes the location of two faults Fault1and Fault2 in Fig. 5, two faults intersect near the coastline and connected to seawater. Borehole cores from Ck12 reveal the presents of Fault1, lower (b) resistivity distribution of B-B'; the start of profile is close to the coastline and the perpendicular with E-E'; White line marked the possible location and front of seawater intrusion. The letters A, B, and C in the profiles denote the location of low resistivity anomalies. (c) Inverted electrical resistivity near the borehole CK12. (d) and (e) Pictures of the core samples from the borehole.

(−70 m below sea surface) provide information about permeability of rocks and seawater intrusion characteristics. Rhyolite-dominated bedrock is typically impermeable (permeability  $k$  smaller than 1 mD,  $1 \text{ D} \approx 10^{-12} \text{ m}^2$ ) unless fault fracture zones serve as the primary conduits for groundwater flow. The insertion of a low resistivity unit into the fault rift zone at 70 m below sea level is considered the strongest evidence of seawater intrusion.

In the western section of the study area, a B-B' resistivity profile spanning approximately 400 m and oriented perpendicular to the coastline in a near north-south direction was reconstructed, as depicted in Fig. 6b. No significant geological structures were observed in comparison to the E-E' profile since the entire B-B' profile lies within the same geological unit. Due to the low permeability of the bedrock, the inverse resistivity model below 0 m is expected to exhibit consistently high resistivity characteristics. However, the southern portion of the B-B' profile, extending 150 m inland to the north, displays low resistivity values (enclosed by the white-lines). This deeper aquifer may serve as a potential area for seawater intrusion, as the high salinity of seawater results in lower resistivity within the region. The presence of hot colors indicating resistivities higher than  $100 \Omega\text{-m}$  indicative of impermeable conditions and the absence of seawater intrusions.

As each profile is intersected, a 3D resistivity model can be reconstructed to provide a comprehensive map of geological structure and aquifer properties. The shallow sections of layered resistivity contrast reveal valuable information about the surficial geological features, such as sediment thickness and the recharge zone of the surface groundwater. Low-resistivity areas in the deeper layers can indicate the presence of fault zones or the existence of a deep saline aquifer influenced by seawater.

Fig. 7a displays resistivity variations within a 5-m range (Slice A), which can be correlated with the distribution of surficial geology. Notably, the contour of approximately  $60 \Omega\text{-m}$  aligns well with the boundaries of fault F2. This level of resistivity contrast enables the depiction of geological sections using TEM. The bedrock surface in the eastern part of the survey area is identified as a resistive material (indicated by the hot colour). The blue colour represents underlying sediments and the recharge zone for water supply. The conductive zone in the northwestern corner near the Menaotu river is likely attributed to ground-water recharge, as mentioned above, this river is connected to

the seawater, the infiltration of high-salinity river water into the ground leads to a reduction in resistivity. However, due to the overlapping resistivity ranges with clay-rich sediments, we were unable to delineate the exact boundary of the recharge zone. Fig. 8b illustrates the resistivity values at a depth of 50 m (slice B), where the conductive zone near the river is not visible. Of particular interest, we observe an oxbow-shaped area of low resistivity extending inland from the coastline, reaching a depth of 50 m, just between the middle zone of two faults. When compared with vertical sections, slice B in plan view provides information regarding the size and geometry of salinity. Seawater primarily infiltrates from the southern part of the island, with the graben and fracture zone situated between the two faults serving as a significant pathway for seawater intrusion.

We compared the conductivity obtained from the TEM data and the pore water experimental data from boreholes. The predicted conductivity near the borehole is obtained through Kriging interpolation. Both conductivity and pH of porewater show a good correlation between predicted conductivity,  $R = 0.93$  and  $R = 0.94$ , respectively (Fig. 8). Although the conductivity of pore water is much higher than that of inversion, TEM detects the bulk conductivity of pore water and rock matrix, and the good correlation between them indicates that the conductivity predicted by TEM can reflect the properties of pore water. In saturated conditions, the conductivity of the rock  $\sigma$  can be written as a function of the conductivity of the pore water  $\sigma_w$  as

$$\sigma = \frac{\sigma_w}{F} + \sigma_s \quad (2)$$

where  $F$  denotes the formation factor and  $\sigma_s$  the surface conductivity associated with conductivity in the electrical double layer. The data of Fig. 8a indicates that  $F \sim 170 \pm 30$  and  $\sigma_s = 4.8 \pm 0.3 \text{ S m}^{-1}$ . These values are associated with the low porosity of the rhyolites and the surface conductivity is associated with their alteration (Revil et al., 2017a, 2017b). They could be considered as average values for the unfractured basement by they would need to be confirmed through petrophysical measurements. The correlation between inversion conductivity and pore water pH indicates that inverted conductivity is correlated with the salinity of pore water. Seawater with high salinity exhibits relatively high pH and high conductivity.

A quasi-3D model could be provided, through the inversion of TEM

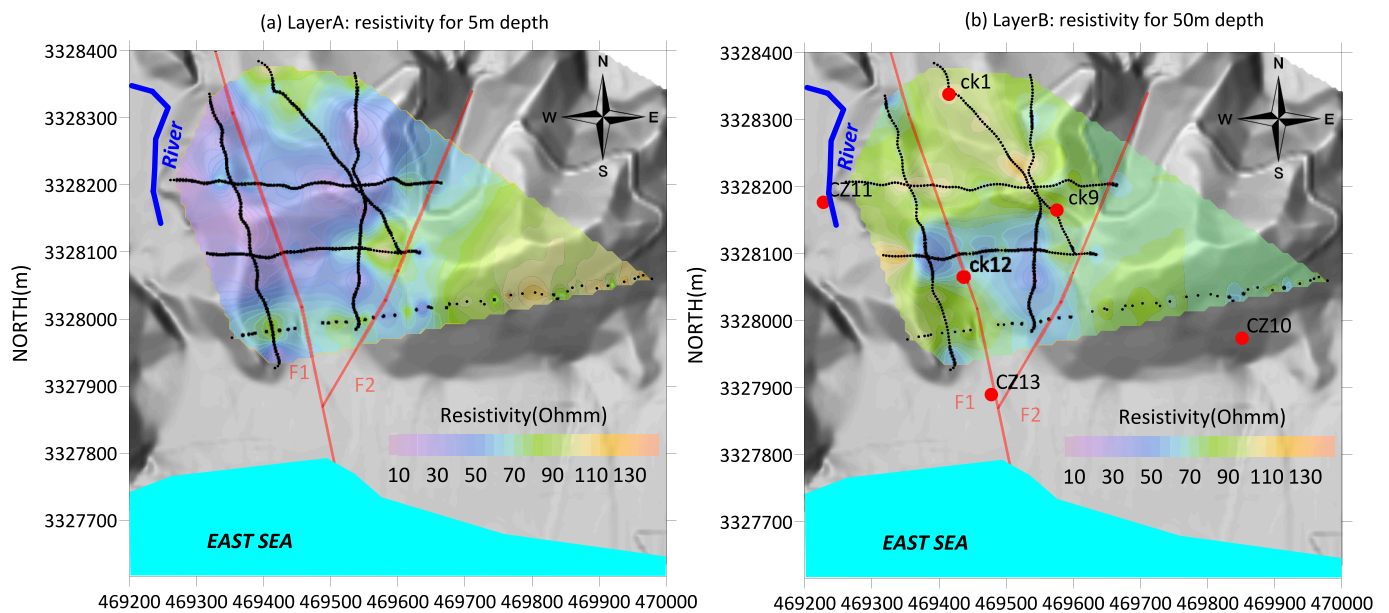
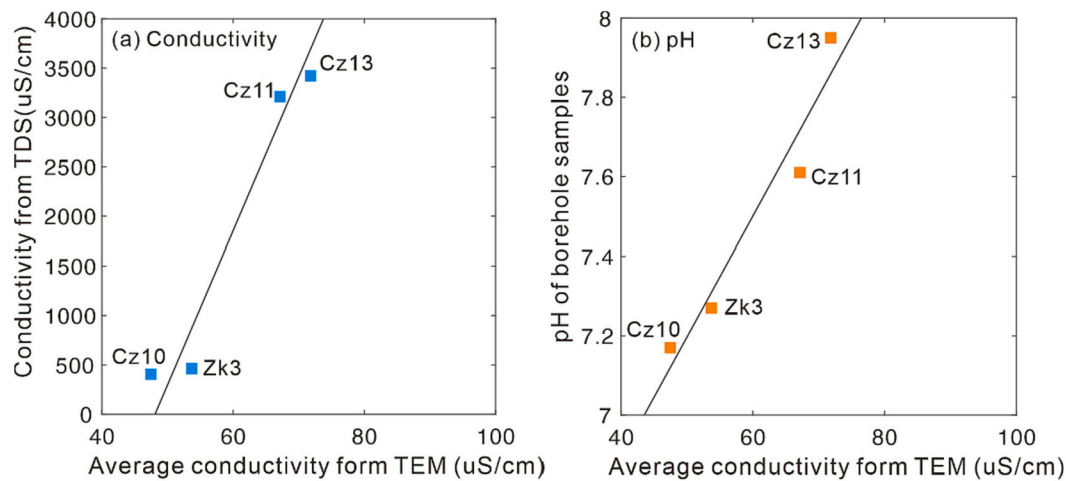
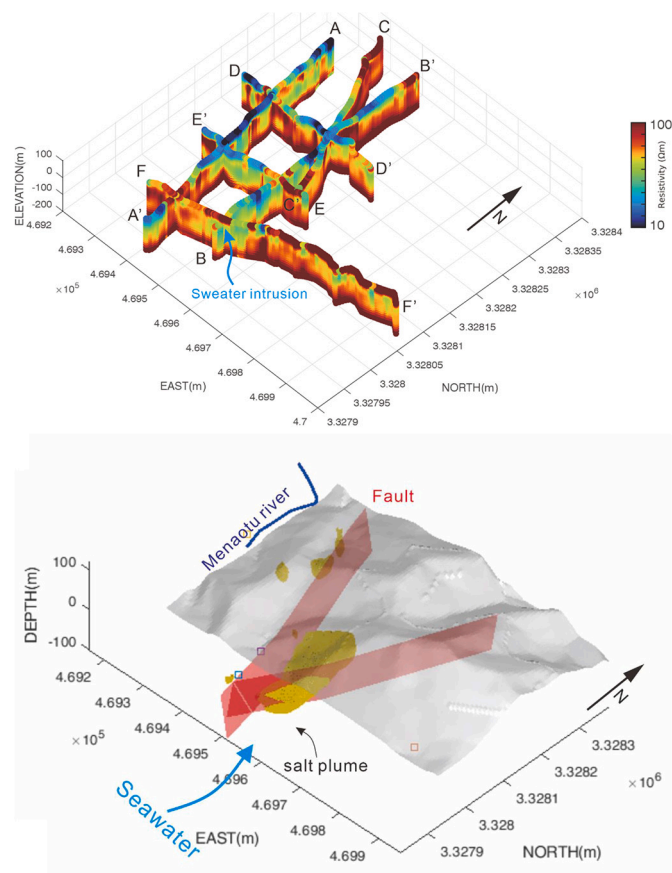


Fig. 7. Plan view of inverted resistivity at different depths. (a) Slice A present the shallow resistivity contrast within a 5 m. (b) Resistivity at depths of 50 m, Slice B; Red solid lines F1 and F2 indicate certain faults, controlled by region geology. (For interpretation of the references to colour in this figure legend, the reader is referred to the web version of this article.)



**Fig. 8.** TEM electrical conductivity versus in situ measurements for the pore water conductivity (in  $\mu\text{S cm}^{-1}$ ) and pH. (a) Relationship between the TEM conductivity versus the pore water conductivity determined from the TDS. (b) Relationship between the TEM conductivity versus the in situ pH values. The pH of the seawater is measured to be higher compared with the pH of the groundwater.

data. The 3D conductivity map is displayed in Fig. 9a showing the high resistive bedrock. Very low resistivity areas are observed in the shallow surface suggesting thicker sediments than anticipated with high water content. Inferred seawater intrusion paths characterized as a low resistivity feature, extending from southern part of islands to the



**Fig. 9.** Inferred salt plume from TEM data. (a). Recovered quasi 3D resistivity model through inversion of TEM data. (b) 3D salt plume volume obtain from reconstructed voxel resistivity, and the red plane denote the location of geology fault. Seawater intrusion is mainly distributed along the cracks present in the rhyolitic substratum. (For interpretation of the references to colour in this figure legend, the reader is referred to the web version of this article.)

northwest side, through the fractured zone of fault between two hills. Fig. 9b show the inferred salt plume from voxel resistivity model, on average, the depth of the saline plume in the results is about 25 m below the sea level. In addition, the fact that CZ13 is located in a fault zone provides a key point to understand the channelling of the salty water in this area. Indeed, fault zones can act as conduits or barriers for fluid flow based on their nature (Revil and Cathles, 2002). In this case, it seems the fault may be serving as a conduit, facilitating the movement of seawater into the groundwater system, especially evident with the high TDS values noted in well CZ13. Transient electromagnetic investigations reveal the low resistivity zone around the faults, provide a potential insight into the dynamics of this seawater intrusion. In the future, we will need to model the effects of the faults into the dynamic of sea water intrusion in this area. We could also use induced polarization to characterize the permeability of the area (see Revil et al., 2020).

**5. Conclusion**

Using a compact transient electromagnetic device, we successfully obtained high-density transient electromagnetic data on a small island in Hangzhou Bay. By incorporating a layered inversion technique with spatially constraints, we reconstruct the three-dimensional resistivity distribution of the islands near the coastal area. Utilizing the lateral discontinuity of resistivity model, we pinpointed the location of the faults and subsequently observed low resistivity zones distributed along these faults. Combined with TDS data analysis of surface and borehole samples, we infer that these low-resistivity zones are closely associated with seawater intrusion. Further imaging results revealed the invasion sites of seawater plumes, suggesting that in hard igneous rock areas, faults and fractured areas serve as the primary channels for seawater intrusion associated with climate change, sea water rise, and the use of wells for pumping fresh water.

**CRedit authorship contribution statement**

**Zhongmin Zhu:** Writing – review & editing, Writing – original draft, Visualization, Validation, Supervision, Software, Resources, Project administration, Methodology, Investigation, Funding acquisition, Formal analysis, Data curation, Conceptualization. **Zhigang Shan:** Writing – review & editing, Writing – original draft, Supervision. **Yonghao Pang:** Writing – review & editing, Writing – original draft, Validation, Methodology, Investigation. **Wei Wang:** Writing – review & editing, Writing – original draft, Methodology, Formal analysis. **Mei Chen:** Writing – review & editing, Writing – original draft, Validation,

Supervision, Project administration, Funding acquisition, Formal analysis, Conceptualization. **Guangchang Li:** Project administration, Methodology. **Huaifeng Sun:** Writing – review & editing, Writing – original draft, Visualization, Validation, Methodology, Investigation, Formal analysis. **André Revil:** Writing – review & editing, Writing – original draft, Supervision, Methodology, Data curation.

### Declaration of competing interest

The authors declare that they have no known competing financial interests or personal relationships that could have appeared to influence the work reported in this paper.

### Data availability

All the data used to generate the figures can be obtained by connecting the corresponding author. The data used also are available on PANGAEA.

### Acknowledgements

This research is funded by foundations from Zhejiang Huadong Construction Engineering CO., LTD (ZKY2022-HDJS-02-02). We thank the Seigo Kang and other developers of SimPEG-EM1D. A. Revil thanks the CNRS for its support over the years. We thank the editor Paolo Frattini and two Referees for their constructive comments.

### References

- Adeyemo, I.A., Oladeji, E.O., Sanusi, S.O., Olayanju, G.M., 2022. Mapping the possible origin of anomalous saline water occurrence in Agbabu, Eastern Dahomey Basin, Nigeria: insights from geophysical and hydrochemical methods. *Results Geophys. Sci.* 10, 100042 <https://doi.org/10.1016/j.ringps.2022.100042>.
- Amer, L., Erkok, M., Feagin, R.A., Kameshwar, S., Mach, K.J., Mitsova, D., 2023. Measuring resilience to sea-level rise for critical infrastructure systems: leveraging leading indicators. *J. Mar. Sci. Eng.* 11 (7), 1421. <https://doi.org/10.3390/jmse11071421>.
- Auken, E., Christiansen, A.V., Westergaard, J.H., Kirkegaard, C., Foged, N., Viezzoli, A., 2009. An integrated processing scheme for high-resolution airborne electromagnetic surveys, the SkyTEM system. *Explor. Geophys.* 40 (2), 184–192. <https://doi.org/10.1071/EG08128>.
- Auken, E., Foged, N., Larsen, J.J., Lassen, K.V.T., Maurya, P.K., Dath, S.M., Eiskjær, T.T., 2019. tTEM - a towed transient electromagnetic system for detailed 3D imaging of the top 70 m of the subsurface. *Geophysics* 84 (1), E13–E22. <https://doi.org/10.1190/geo2018-0355.1>.
- Auken, E., Foged, N., Andersen, K.R., Nyboe, N.S., Christiansen, A.V., 2020. On-time modelling using system response convolution for improved shallow resolution of the subsurface in airborne TEM. *Explor. Geophys.* 51 (1), 4–13. <https://doi.org/10.1080/08123985.2019.1662292>.
- Barlow, P.M., 2003. Ground water in freshwater-saltwater environments of the Atlantic coast. *US Geol. Surv. Circ.* 1262, 1–113.
- Bense, V.F., Person, M.A., 2006. Faults as conduit-barrier systems to fluid flow in siliciclastic sedimentary aquifers. *Water Resour. Res.* 42 <https://doi.org/10.1029/2005WR004480>.
- Binley, A., Hubbard, S.S., Huisman, J.A., Revil, A., Robinson, D.A., Singha, K., Slater, L. D., 2015. The emergence of hydrogeophysics for improved understanding of subsurface processes over multiple scales. *Water Resour. Res.* 51, 3837–3866. <https://doi.org/10.1002/2015WR017016>.
- Christensen, N.B., 2014. Sensitivity functions of transient electromagnetic methods. *Geophysics* 79 (4), E167–E182. <https://doi.org/10.1190/geo2013-0364.1>.
- Cockett, R., Kang, S., Heagy, L.J., Pidlisceky, A., Oldenburg, D.W., 2015. SimPEG: an open source framework for simulation and gradient based parameter estimation in geophysical applications. *Comput. Geosci.* 85 (Part A), 142–154. <https://doi.org/10.1016/j.cageo.2015.09.015>.
- Delsman, J.R., Van Baaren, E.S., Siemon, B., Dabekaussen, W., Karaoulis, M.C., Pauw, P. S., Vermaas, T., Bootsma, H., De Louw, P.G., Gunnink, J.L., Dubelaar, C.W., 2018. Large-scale, probabilistic salinity mapping using airborne electromagnetics for groundwater management in Zeeland, the Netherlands. *Environ. Res. Lett.* 13 (8), 084011 <https://doi.org/10.1088/1748-9326/aad19e>.
- Dhal, L., Swain, S., 2022. Understanding and modeling the process of seawater intrusion: a review. In: *Advances in Remediation Techniques for Polluted Soils and Groundwater*, pp. 269–290. <https://doi.org/10.1016/B978-0-12-823830-1.00009-2>.
- Goebel, M., Knight, R., Halkjær, M., 2019. Mapping saltwater intrusion with an airborne electromagnetic method in the off shore coastal environment, Monterey Bay, California. *J. Hydrol. Region. Stud.* 23 (March), 100602 <https://doi.org/10.1016/j.ejrh.2019.100602>.
- Gottschalk, I., Knight, R., Asch, T., Abraham, J., Cannia, J., 2020. Using an airborne electromagnetic method to map saltwater intrusion in the northern Salinas Valley, California. *Geophysics* 85 (4), B119–B131. <https://doi.org/10.1190/geo2019-0272.1>.
- Heagy, L.J., Cockett, R., Kang, S., Rosenkjaer, G.K., Oldenburg, D.W., 2017. A framework for simulation and inversion in electromagnetics. *Comput. Geosci.* 107, 1–19. <https://doi.org/10.1016/j.cageo.2017.06.018>.
- Kalisperi, D., Kouli, M., Vallianatos, F., Soupios, P., Kershaw, S., Lydakis-Simantiris, N., 2018. A transient electromagnetic (TEM) method survey in north-central coast of Crete, Greece: evidence of seawater intrusion. *Geosci. (Switzerland)* 8 (4). <https://doi.org/10.3390/geosciences8040107>.
- Kang, S., Knight, R., Goebel, M., 2022. Improved imaging of the large-scale structure of a groundwater system with airborne electromagnetic data. *Water Resour. Res.* 58 (4) <https://doi.org/10.1029/2021WR031439>.
- Knight, R., Steklova, K., Miltenberger, A., Kang, S., Goebel, M., Fogg, G., 2022. Airborne geophysical method images fast paths for managed recharge of California's groundwater. *Environ. Res. Lett.* 17 (12) <https://doi.org/10.1088/1748-9326/aca344>.
- Kumar, P., Mukherjee, S., 2023. Impact of limestone caves and seawater intrusion on coastal aquifer of middle Andaman. *J. Contam. Hydrol.* 256, 104197 <https://doi.org/10.1016/j.jconhyd.2023.104197>.
- Kura, N.U., Ramli, M.F., Ibrahim, S., Sulaiman, W.N.A., Aris, A.Z., 2014. An integrated assessment of seawater intrusion in a small tropical island using geophysical, geochemical, and geostatistical techniques. *Environ. Sci. Pollut. Res.* 21 (11), 7047–7064. <https://doi.org/10.1007/s11356-014-2598-0>.
- Lane, J.W., Briggs, M.A., Maurya, P.K., White, E.A., Pedersen, J.B., Auken, E., Terry, N., Minsley, B., Kress, W., LeBlanc, D.R., Adams, R., Johnson, C.D., 2020. Characterizing the diverse hydrogeology underlying rivers and estuaries using new floating transient electromagnetic methodology. *Sci. Total Environ.* 740, 140074 <https://doi.org/10.1016/j.scitotenv.2020.140074>.
- Lo, M., Sangare, D., 2023. Parametrical study of freshwater–saltwater interface dynamic. In: *Modelling and Simulation in Engineering*, pp. 1–11. <https://doi.org/10.1155/2023/2715152>.
- Luo, Z., Kong, J., Yu, X., Lu, C., Werner, A.D., Barry, D.A., 2023. Effects of unsaturated flow on salt distributions in tidally influenced coastal unconfined aquifers. *Water Resour. Res.* 59, 6. <https://doi.org/10.1029/2022WR032931>.
- Maurya, P.K., Christiansen, A.V., Pedersen, J., Auken, E., 2020. High resolution 3D subsurface mapping using a towed transient electromagnetic system – tTEM: case studies. *Near Surf. Geophys.* 18 (3), 249–259. <https://doi.org/10.1002/nsg.12094>.
- Panthi, J., Pradhanang, S.M., Nolte, A., Boving, T.B., 2022. Saltwater intrusion into coastal aquifers in the contiguous United States — a systematic review of investigation approaches and monitoring networks. *Sci. Total Environ.* 836, 155641. <https://doi.org/10.1016/j.scitotenv.2022.155641>.
- Qasim, A., Singh, S.P., Chandrashekar, A.K., 2022. Chandrashekar, Geochemical and isotope tracing of groundwater salinity in the coastal Gujarat alluvial plain, India. *J. Contam. Hydrol.* 248, 104000. <https://doi.org/10.1016/j.jconhyd.2022.104000>.
- Revil, A., Cathles, L.M., 2002. Fluid transport by solitary waves along growing faults: a field example from the South Eugene Island Basin, Gulf of Mexico. *Earth Planet. Sci. Lett.* 202 (2), 321–335 (erratum: Revil, A. and L.M., Cathles, 2002, Fluid transport by solitary waves along growing faults: a field example from the South Eugene Island Basin, Gulf of Mexico, *Earth and Planetary Science Letters*, 204(1–2), 321–322).
- Revil, A., Cary, L., Fan, Q., Finizola, A., Trolard, F., 2005. Self-potential signals associated with preferential ground water flow pathways in a buried paleo-channel. *Geophys. Res. Lett.* 32, L07401. <https://doi.org/10.1029/2004GL022124>.
- Revil, A., Le Breton, M., Niu, Q., Wallin, E., Haskins, E., Thomas, D.M., 2017a. Induced polarization of volcanic rocks. 1. Surface versus quadrature conductivity. *Geophys. J. Int.* 208, 826–844. <https://doi.org/10.1093/gji/ggw444>.
- Revil, A., Le Breton, M., Niu, Q., Wallin, E., Haskins, E., Thomas, D.M., 2017b. Induced polarization of volcanic rocks. 2. Influence of pore size and permeability. *Geophys. J. Int.* 208, 814–825. <https://doi.org/10.1093/gji/ggw382>.
- Revil, A., Soueid Ahmed, A., Coperey, A., Ravanel, L., Sharma, R., Panwar, N., 2020. Induced polarization as a tool to characterize shallow landslides. *J. Hydrol.* 589, 125369 <https://doi.org/10.1016/j.jhydrol.2020.125369>.
- Sandersen, P.B.E., Kallesøe, A.J., Møller, I., Høyer, A.S., Jørgensen, F., Pedersen, J.B., Christiansen, A.V., 2021. Utilizing the towed Transient ElectroMagnetic method (tTEM) for achieving unprecedented near-surface detail in geological mapping. *Eng. Geol.* 288 <https://doi.org/10.1016/j.enggeo.2021.106125>.
- Seibert, S.L., Greskowiak, J., Bungenstock, F., Freund, H., Karle, M., Meyer, R., Oude Essink, G.H.P., Engelen, J., Massmann, G., 2023. Paleo-hydrogeological modeling to understand present-day groundwater salinities in a low-lying coastal groundwater system (Northwestern Germany). *Water Resour. Res.* 59, 4. <https://doi.org/10.1029/2022WR033151>.
- Sharan, A., Lal, A., Datta, B., 2023. Evaluating the impacts of climate change and water over-abstraction on groundwater resources in Pacific island country of Tonga. *Groundw. Sustain. Dev.* 20, 100890 <https://doi.org/10.1016/j.gsd.2022.100890>.
- Viezzoli, A., Auken, E., Munday, T., 2009. Spatially constrained inversion for quasi 3D modelling of airborne electromagnetic data an application for environmental assessment in the lower Murray Region of South Australia. *Explor. Geophys.* 40 (2), 173–183. <https://doi.org/10.1071/EG08027>.
- Wang, Z., Chen, H., Li, F., Wang, G., 2022. Experimental and simulation study on the impact of storage and recovery of coastal aquifer to seawater intrusion. *Nat. Hazards* 114 (1), 237–259. <https://doi.org/10.1007/s11069-022-05388-7>.
- Yin, C., Smith, R.S., Hodges, G., Annan, P., 2008. Modeling results of On- and Off-time B and dB/dt for time-domain airborne EM systems. In: 70th EAGE Conference & Exhibition. <https://doi.org/10.3997/2214-4609.20147788>.